Applied Catalysis B: Environmental 174–175 (2015) 445–454

Contents lists available at ScienceDirect

Applied Catalysis B: Environmental

journal homepage: www.elsevier.com/locate/apcatb

Synthesis and applications of novel graphitic carbon nitride/metal-organic frameworks mesoporous photocatalyst for dyes removal

Hou Wang[a,b], Xingzhong Yuan[a,b,c,*], Yan Wu[d], Guangming Zeng[a,b], Xiaohong Chen[c], Lijian Leng[a,b], Hui Li[e]

[a] College of Environmental Science and Engineering, Hunan University, Changsha 410082, PR China
[b] Key Laboratory of Environment Biology and Pollution Control, Hunan University, Ministry of Education, Changsha 410082, PR China
[c] Collaborative Innovation Center of Resource-Conserving & Environment-Friendly Society and Ecological Civilization, Changsha 410083, PR China
[d] College of Environment and Energy, South China University of Technology, Guangzhou 510006, PR China
[e] Institute of Bio-Energy, Hunan Academy of Forestry, Changsha 410004, PR China

ARTICLE INFO

Article history:
Received 3 February 2015
Received in revised form 16 March 2015
Accepted 22 March 2015
Available online 24 March 2015

Keywords:
Metal-organic frameworks
Graphitic carbon nitride
Photocatalysis
Heterostructures
Visible-light

ABSTRACT

Metal-organic frameworks (MOFs) have been attracted considerable attention for their applications in gas storage/separation, adsorption as well as catalysis. In this study, a facile solvothermal method was employed to prepare MOFs and graphitic carbon nitride (g-C_3N_4) hybrids, and a g-C_3N_4/Ti-benzenedicarboxylate (MIL-125(Ti)) heterostructures photocatalyst was successfully synthesized. The as-obtained materials were characterized by field emission scanning electron microscopy (FESEM), transmission electron microscopy (TEM), X-ray diffraction (XRD), N_2 adsorption–desorption isotherm, thermogravimetric analysis (TGA), X-ray photoelectron spectroscopy (XPS), UV–vis diffuse reflection spectroscopy (UV–vis DRS), and photoluminescence (PL) spectroscopy. It is indicated that the hybrids have large surface area, mesoporous structure, thermal stability, and enhanced visible-light absorption. Compared with pure MIL-125(Ti) and g-C_3N_4, the composites exhibited more efficient photocatalytic performance for Rhodamine B degradation from aqueous solution under visible-light irradiation. The optimal g-C_3N_4 content in g-C_3N_4/MIL-125(Ti) composite was determined to be 7.0 wt%, and the corresponding photodegradation rate for RhB was 0.0624 min^{-1}, about 2.1 and 24 times higher than that of pure g-C_3N_4 and MIL-125(Ti), respectively. The indirect dye photosensitization, the Ti^{3+}–Ti^{4+} intervalence electron transfer, and the synergistic effect between MIL-125(Ti) and g-C_3N_4 were the three reasons for improved photo-degradation performance. Therefore, it is reasonable to believe that metal-free semiconductor/MOFs photocatalysts have great potentiality in environmental remediation.

© 2015 Elsevier B.V. All rights reserved.

1. Introduction

Photocatalysis, a highly important route to solar-to-chemical energy conversion, has been widely studied for environment cleaning and for energy production [1–3]. In photocatalysis technology, semiconductor materials are excited by light absorption to produce electron–hole pairs which are then separated and transferred to target object for redox reactions [4]. Metal-organic frameworks (MOFs), consisting of organic linkers and metal–oxo clusters, have intriguing crystalline structures, tailorable chemistry, large specific surface area, and well-defined porosity [5,6]. Consequently, much attention has been paid to potential applications of MOFs in gas capture and storage, chemical separation, sensor devices, drug delivery, and catalysis [7–12]. Nevertheless, the performance of MOFs served as photocatalysts in photocatalysis is not comparable to that of inorganic semiconductors due to the low efficiency for solar energy conversion and photo-generated charge separation.

Compared with pure MOFs, the heterostructures integrating MOFs with metal oxide/sulfides (CdS [3], TiO_2 [13], SiO_2 [14], Fe_3O_4 [15], ZnO [12], and Cu_2O [16]) or metals (Au [17], Pt [2,18,19], Pd [20], and AuNi alloy [21]) acted as catalysts show great advantages due to their synergism effect. Our previous research indicated that graphene oxide (GO) could enhance the catalytic efficiency of MOF catalysts for the degradation of dyes [22]. He et al. manifested that

* Corresponding author at: College of Environmental Science and Engineering, Hunan University, Changsha 410082, PR China. Tel.: +86 731 88821413; fax: +86 731 88823701.
E-mail address: yxz@hnu.edu.cn (X. Yuan).

http://dx.doi.org/10.1016/j.apcatb.2015.03.037
0926-3373/© 2015 Elsevier B.V. All rights reserved.

the photocatalytic hydrogen production efficiency of CdS nanoparticles embedded on MIL-101 under visible-light irradiation was superior to bare CdS due to a large specific surface area, more active adsorption sites, and photocatalytic reaction centers, good visible-light harvesting capability [3]. A "double solvents" approach for the incorporation of Pt nanoparticles within pores of MIL-101 had been developed by Arshad et al. [19]. The Pt/MOFs exhibited excellent catalytic performances for liquid-phase ammonia borane hydrolysis, solid-phase ammonia borane thermal dehydrogenation, and gas-phase CO oxidation. Although the photocatalytic activity of MOFs modified by the functionalized materials has been improved, the system still suffers from many limitations including high cost, complicated synthesis process, or instability during photochemical operations.

Different from metal compound photocatalyst, graphite-like carbon nitride (g-C_3N_4) is a metal-free semiconductor and can be synthesized by a simple heating of urea, melamine, or cyanamide [1,23,24]. In addition, the cheap g-C_3N_4 semiconductor can absorb visible-light due to the band gap of 2.70 eV and is stable in solutions with pH 0–14 under light irradiation. These superior performances make the metal-free g-C_3N_4 have great potentiality in the field of photocatalysis. However, high recombination rate of e^-–h^+ pair in g-C_3N_4 is one of the major factors limiting its photocatalytic efficiency. Coupling with inorganic materials (such as TiO_2, Zn_2GeO_4, $SmVO_4$, Ag_2O, *etc.*) with suitable band potential is a feasible route to lower the recombination rate and improve the photocatalytic activity [1,23,25–30]. Graphitic C_3N_4 improves the photoactivity of semiconductor from two aspects: (i) effective charge carrier separation; (ii) good sensitizer for visible-light responding. For instance, Wang et al. highlighted the g-C_3N_4-redox catalysis promoted by cobalt-containing zeolitic imidazolate framework (Co-ZIF-9) for CO_2 reduction upon visible-light illumination at mild reaction conditions [30]. Graphitic C_3N_4 served as a semiconductor photocatalyst, whereas, Co-ZIF-9 was a co-catalyst that facilitated the CO_2 adsorption and light-induced charge separation. Li et al. reported an organic–inorganic composite photocatalyst of g-C_3N_4/$SmVO_4$ that showed a higher photocatalytic activity than either the single-phase g-C_3N_4 or $SmVO_4$ [1]. Pan et al. fabricated core/shell structured C_3N_4/$BiPO_4$ photocatalyst *via* a facile ultrasonic dispersion method [29]. After introduction of C_3N_4, the photocatalytic activity of C_3N_4/$BiPO_4$ photocatalyst was almost 4.5 times as high as that of reference P25 (TiO_2) and 2.5 times of $BiPO_4$ under UV light irradiation, which was due to the match of lattice and energy level between the C_3N_4 and $BiPO_4$. However, the report about the synthesis and applications of metal-free semiconductor/MOFs heterostructures is still scarce.

MIL-125 or $Ti_8O_8(OH)_4$–$(O_2C$–C_6H_4–$CO_2)_6$, a highly porous and crystalline titanium dicarboxylate with a high thermal stability and photochemical properties, owns large surface area and accessible pore diameters [31]. This material can not only introduce high density of the immobilized Ti sites within porous MOFs, but also synthesize isostructural MOFs with improved photocatalytic properties by tuning the incorporation of organic ligands [32]. We have also previously reported the synthesis of a visible-light responsive amino-functionalized Ti-benzenedicarboxylate by employing 2-amino-benzenedicarboxylic acid as an organic linker, and the application in photocatalytic Cr(VI) reduction from water under visible-light irradiation [33]. MIL-125 also exhibits a photochromic behavior associated with the formation of stable mixed valence titanium–oxo compounds [34]. In this paper, metal-free g-C_3N_4/MIL-125(Ti) hybrids were designed by a facile one-pot solvothermal method. The resultant g-C_3N_4/MIL-125(Ti) (CMTi) heterostructures photocatalysts were characterized comprehensively by means of XRD, FESEM, TEM, XPS, N_2 adsorption–desorption isotherm, UV–vis DRS, and PL spectroscopy. By optimizing the compositions, an environmental-friendly composite was found to show superior photocatalytic activity towards Rhodamine B dye degradation under visible-light irradiation. The photocatalytic mechanism as well as the reusability and stability of photocatalyst were also investigated.

2. Experimental

2.1. Materials

Dicyandiamide ($C_2H_4N_4$), tetrabutyl titanate (TBT; $C_{16}H_{36}O_4Ti$), 1,4-benzenedicarboxylic acid (BDC; $C_8H_6O_4$), *N′N*-dimetylformanide (DMF; $(CH_3)_2NCHO$)), methanol (CH_3OH), ethylenediaminetetraacetic acid disodium salt (EDTA-2Na), *p*-benzoquinone, and isopropyl alcohol were purchased from Sinopharm Chemical Reagent Co., Ltd. (Shanghai, China). All reagents and solvents were of analytical reagent grade and used as received from commercial suppliers.

2.2. Synthesis of g-C_3N_4/MIL-125(Ti) hybrids

The g-C_3N_4 was prepared by calcination with dicyandiamide as precursor. Typically, 10 g of dicyandiamide was put into a crucible with a cover, and then heated at 550 °C in a muffle furnace for 4 h with a heating rate of 10 °C min^{-1}. The resultant yellow powder was collected for further use. The g-C_3N_4/MIL-125(Ti) composite was synthesized according to a modified method [33]. A certain amount of g-C_3N_4 powder was dispersed into DMF with the aid of ultrasonication. Then a mixture of TBT (2.4 mL), BDC (2.2 g), g-C_3N_4/DMF mixture (36 mL), and methanol (4.0 mL) was subjected to solvothermal conditions in a Teflon-lined stainless-steel autoclave for 48 h at 150 °C. After reaction, the resultant precipitate was separated by centrifugation, washed repeatedly with DMF and methanol. Finally, the samples were dried at 80 °C under vacuum. The as-obtained hybrids were denoted as CMTi-1, CMTi-2, CMTi-3, and CMTi-4. For comparison purposes, conventional MIL-125(Ti) was prepared in the absence of g-C_3N_4 under the same conditions.

2.3. Characterization

Thermogravimetric analysis (TGA) curves were measured by using a SDT Q600 thermogravimetric analyzer from room temperature to 800 °C with heating rate of 10 °C min^{-1} and an air flow rate of 100 mL min^{-1}. The powder X-ray diffraction (XRD) patterns were recorded using Bruker AXS D8 advance diffractometer operating with Cu-K*a* source to investigate the crystal structure of the samples. The morphologies of resulting samples were characterized by a field emission scanning electron microscopy (SEM) (JSM-7001F, Japan) and transmission electron microscopy (TEM) (JES-3010, Japan). The surface electronic state was analyzed by X-ray photoelectron spectroscopy (Thermo Fisher Scientific, UK). The specific surface area of these samples was characterized from the nitrogen absorption–desorption data and Brunauer–Emmett–Teller (BET) measurement (ASAP2020, Micromeritics, USA). UV–vis diffuse-reflectance spectra (UV–vis DRS) of as-synthesized samples were recorded in the range of 200–800 nm with a Varian Cary 300 spectrometer equipped with an integrating sphere. Photoluminescence (PL) spectroscopy was measured at the excitation wavelength of 320 nm on PerkinElmer LS-55 spectrofluorimeter at room temperature. The total organic carbon (TOC) assays were carried out using a Shimadzu TOC-VCPH analyzer.

2.4. Photocatalytic experiment

Photocatalytic degradation of RhB was carried out in a 250 mL beaker containing 100 mL RhB solution (50 mg L^{-1}) and photocatalyst (40 mg). The solution was magnetically stirred in a darkroom

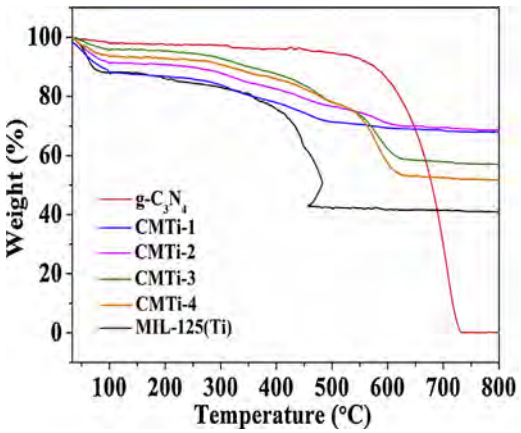

Fig. 1. Thermal analysis of g-C_3N_4, MIL-125(Ti) and CMTi composite under air atmosphere.

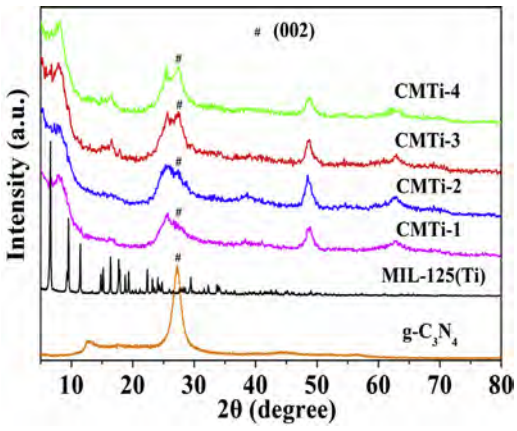

Fig. 2. XRD patterns of g-C_3N_4, MIL-125(Ti) and CMTi composites.

for 60 min to get adsorption–desorption equilibrium. The solution was then irradiated under visible-light illumination ($\lambda > 420$ nm). A 300 W Xenon lamp (Beijing China Education Au-light, Co., Ltd.) with a 420 nm cutoff filter was used as the visible-light source. At certain time intervals, 4 mL aliquots were sampled and centrifuged to remove the particles. The residual RhB concentration was determined using a UV–vis spectrophotometer (UV-2250, SHIMADZU Corporation, Japan) at the wavelength of 554 nm.

3. Results and discussion

3.1. Thermogravimetric analysis

To determine the g-C_3N_4 contents in the final products, thermogravimetric analysis was performed from 40 °C to 800 °C in air. As shown in Fig. 1, pure MIL-125(Ti) shows the main weight loss between 340 °C and 500 °C, corresponding to the degradation of the framework to produce thermal-stable TiO_2. Pure g-C_3N_4 presents the rapid weight loss from 542 °C to 733 °C, indicating the sublimation and/or decomposition of g-C_3N_4. As for CMTi composites, the weight decreases *via* three stages. The weight loss from 45 °C to 100 °C is the departure of the guest molecules methanol or H_2O. The main weight loss between 340 °C and 500 °C is ascribed to the pyrolysis of MIL-125(Ti) while the weight changes from 542 °C to 733 °C are due to the loss of g-C_3N_4. From TGA, the content of g-C_3N_4 in CMTi-1, CMTi-2, CMTi-3, and CMTi-4 was *ca.* 3.8, 7.0, 22.4 and, 27.6 wt%, respectively.

3.2. Structure and morphology analysis

The X-ray diffraction patterns of the parent materials and hybrids are presented in Fig. 2. The pattern of MIL-125(Ti) is consistent with those reported in the literatures [32,34,35], demonstrating that this MOF is successfully prepared. The typical (0 0 2) interlayer-stacking peak at 27.2° corresponds to an interlayer distance of ~0.32 nm for g-C_3N_4 [24]. In the case of the hybrids, almost all of the diffraction peaks of CMTi are the same as those of MIL-125(Ti) and g-C_3N_4. Interestingly, new peaks at 7.8°, 25.5°, and 62.9° appear and the peak at 48.6° shows higher intensity. Some peaks disappear and some new peaks emerge in these hybrids as compared with pure MIL-125(Ti), when g-C_3N_4 is introduced. These changes may be attributed to that graphene-like C_3N_4 causes the change of lattice structure and morphology of MIL-125(Ti). Similar changes of XRD patterns had also been found in graphene/MOFs composites [36–39]. The presence of graphene oxide in MOF-5/GO hybrids increased the distortion in the MOF-5 cubic arrangement due to the additional constraints in the degrees of freedom during the synthesis [36]. Both g-C_3N_4 and 1,4-benzenedicarboxylic acid are π-rich structures, there should be strong π–π interactions between them. In the presence of g-C_3N_4 sheets may unusually bend the 1,4-benzenedicarboxylic acid linker, which results in severe twisting of the $TiO_5(OH)$ paddle wheel from an ideal octahedral square grid. Due to this distortion, the MOF crystals crystallize in a bodycentered unit cell instead of a primitive cell with symmetry [31,40]. Therefore, the introduction of g-C_3N_4 affects the crystallization of MOFs and controls the shapes of such heterostructures.

The texture of g-C_3N_4/MIL-125(Ti) can be observed *via* SEM images presented in Fig. 3. For comparison, SEM images of pure g-C_3N_4 and MIL-125(Ti) are also included. It can be seen that g-C_3N_4 samples (Fig. 3(a) and (b)) exhibited an aggregated, slate-like, and smooth particles consisting of lamellar structures. In the latter sample, the plate-like crystals of MIL-125(Ti) (Fig. 3(c) and (d)) are clearly visible with some traces of amorphous phase. The SEM image of CMTi-2 (Fig. 3(e) and (f)) reveals the agglomeration morphology and the attachment of MIL-125(Ti) particles with different shapes on the rough surfaces of g-C_3N_4. Moreover, the surface of particles is less smooth than that for the pure MIL-125(Ti) which may be due to the presence of g-C_3N_4 nanosheets "covering" the MIL-125(Ti) particles [41]. Fig. 4 shows the TEM micrographs of pure g-C_3N_4, pure MIL-125(Ti), and CMTi-2. It can be observed that g-C_3N_4 (Fig. 4(a)) displays two dimensional and overlap lamellar structures whereas, pure MIL-125(Ti) (Fig. 4(b)) shows upright and plate-like particles with an average particle size of 0.6 μm. For the CMTi-2 (Fig. 4(c) and (d)), the irregular MIL-125(Ti) particles covered with bits of g-C_3N_4 nanosheets are found to be embedded in the wrinkling g-C_3N_4 lamellar structure. Herein, combining the XRD, SEM, and TEM analysis, it can be demonstrated that the heterojunction between MIL-125(Ti) and g-C_3N_4 forms, which expects to facilitate the transfer of photo-generated charge carriers. Meanwhile, in the presence of g-C_3N_4 controls the crystallization and morphology of MIL-125(Ti).

3.3. Chemical states analysis

XPS measurement was carried out to obtain the information on chemical state and surface chemical composition of CMTi-2. In Fig. 5(a), a survey spectrum indicates the peaks of Ti, O, C, and N element in CMTi-2 while only the peaks of Ti, O, and C appear in pure MIL-125(Ti). The C 1s spectrum of CMTi-2 sample (Fig. 5(b)) displays five peaks centering at 284.4, 284.5, 286.2, 288.1, and 288.8 eV. The peak at 284.4 and 284.5 eV can be ascribed to sp^2-bonded carbon (C—C bond) and C—H bond [42,43], and the peaks at 286.2 and 288.1 eV can be assigned to the C—N—C and C—$(N)_3$ groups of g-C_3N_4 [44,45], respectively. Another C 1s peak

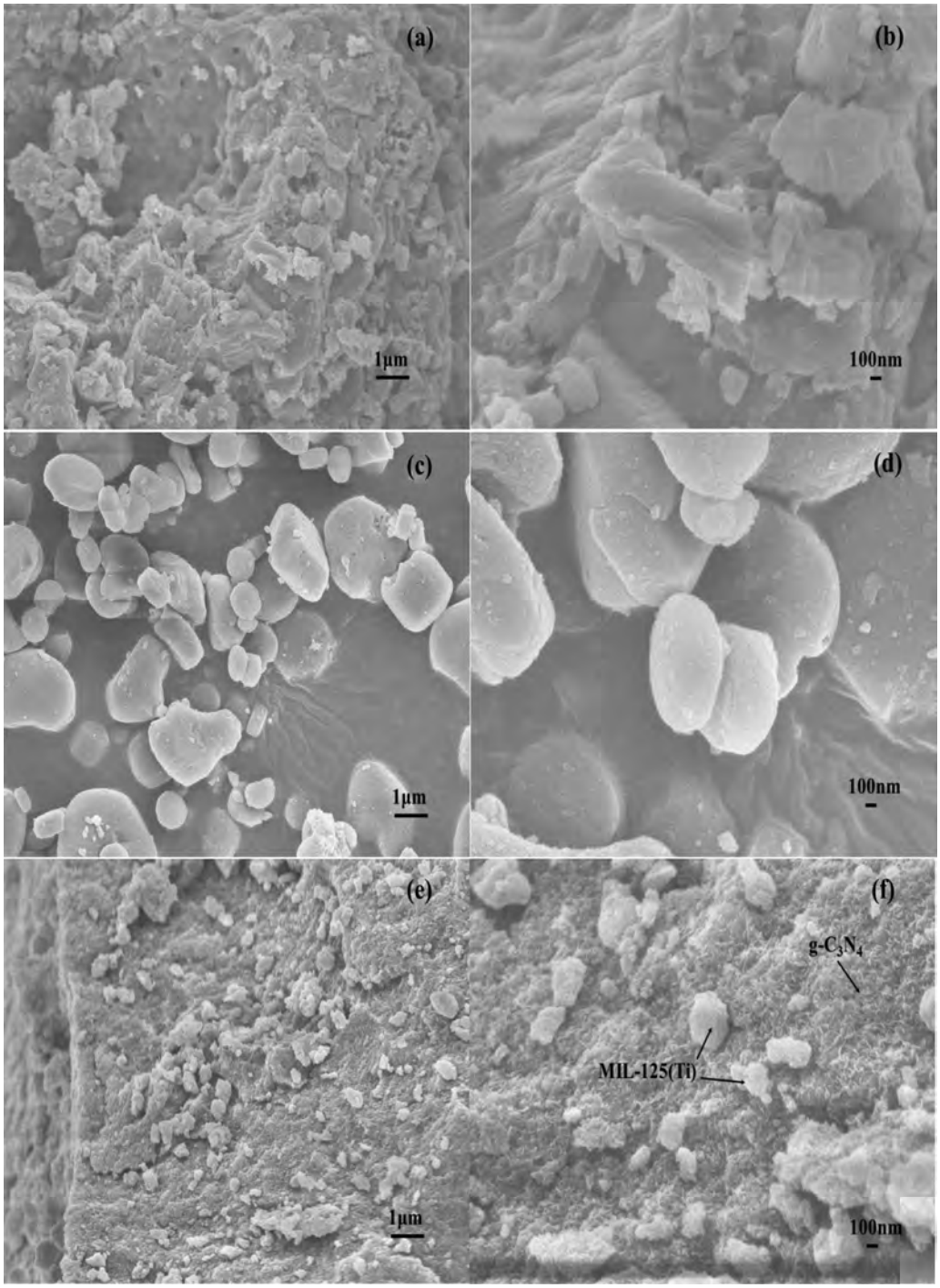

Fig. 3. SEM images of low and high magnification images for (a and b) g-C_3N_4, (c and d) MIL-125(Ti), and (e and f) CMTi-2, respectively.

found at higher energy (288.8 eV) is attributed to O—C=O species [46,47]. The regional spectrum of N 1s for CMTi-2 is also presented in Fig. 5(c). The spectrum can be deconvoluted into four peaks, ascribable to Ti—N bands at 396.6 eV, C—N=C at 398.4 eV, N—$(C)_3$ at 399.9 eV, and graphitic-N species at 402.1 eV [48,49].

Fig. 5(d) shows Ti 2p spectra of MIL-125(Ti) in comparison with that of CMTi-2. The binding energy values of Ti $2p_{3/2}$ and Ti $2p_{1/2}$ at 458.8 and 464.5 eV, respectively, indicate that titanium bounded to oxygen remains in oxidation state IV for the titanium–oxo cluster [33]. However, the shift of 0.4 eV to the lower binding energies of 458.4 and 464.1 eV, respectively, is observed for CMTi-2. This negative shift can be resulted from an enhanced partial electron transformation from N to Ti, and an increased electron density on Ti because of the electronegativity effect between Ti and possibly N atom [44,50]. It is also supported by the peak of Ti—N in N 1s region. The O 1s spectrum (Fig. 6(e)) of MIL-125(Ti) can be fitted into two peaks, and the binding energies of 530.4 and 532.1 eV can be ascribed to oxygen in titanium–oxo cluster and hydroxyl groups, respectively. In comparison with pure MIL-125(Ti), a negative shift of the O 1s to 530.0 and 531.7 eV, with an order of 0.4 eV, is also observed for the CMTi-2 sample. The shift order of O 1s energy position is the same as that of the Ti 2p peak position, implying the incorporation of nitrogen in MIL-125(Ti) [42]. These results are also

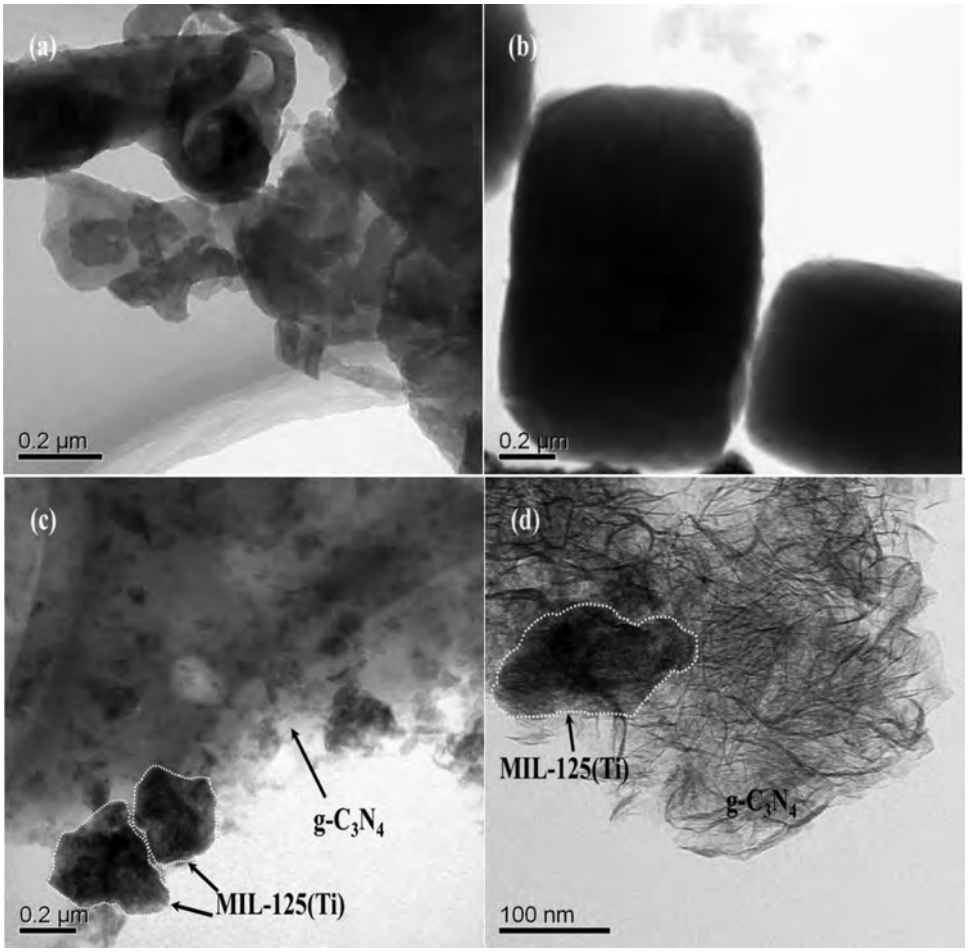

Fig. 4. TEM micrographs of (a) pure g-C_3N_4, (b) pure MIL-125(Ti), and (c and d) CMTi-2.

the proofs for the formation of g-C_3N_4/MIL-125(Ti) heterostructures.

3.4. Specific surface area and optical property

The N_2 adsorption–desorption isotherms on the photocatalyst samples are shown in Fig. 6 and the full data are also shown in Table S1 and Fig. S2. The BET surface area of bare g-C_3N_4 and MIL-125(Ti) is found to be 6.2 $m^2\ g^{-1}$ and 1548.3 $m^2\ g^{-1}$, respectively, while that of CMTi-2 is 328.0 $m^2\ g^{-1}$, which is lower than that of pure MIL-125(Ti) but higher than pure g-C_3N_4. The average pore diameter of CMTi-2 is 6.762 nm, indicating the formation of mesoporous materials. The UV–vis DRS analysis was conducted to assess the optical property of as-prepared MIL-125(Ti), g-C_3N_4, and CMTi composites. As illustrated in Fig. 7(a), pure g-C_3N_4 absorbs the light from the UV to visible-light, and its band gap absorption edge is around 460 nm, while no obvious absorption peak in the visible spectrum is detected for MIL-125(Ti). As for CMTi composite, a notable absorption extension in the visible-light region can be observed due to the g-C_3N_4 serving as the visible-light sensitizer. Additionally, as the content of g-C_3N_4 in the hybrids increases, the optical absorption intensity enhances. It is also indicated that the g-C_3N_4 and the MIL-125(Ti) combine together to form heterojunction, leading to the ability to absorb the visible-light because of the interactions between both components. The red shift of absorption wavelength suggests that these composites can absorb visible-light and be applied for visible-light photocatalysis [3,51,52].

Table 1
Estimated values of energy band gaps (E_g) and adsorption quantity of the photocatalysts.

Samples	E_g (eV)	Adsorption quantity (mg RhB/g catalyst)
MIL-125(Ti)	3.68	4.2
CMTi-1	3.28	30.3
CMTi-2	3.24	49.5
CMTi-3	3.46	48.7
CMTi-4	3.50	30.8
g-C_3N_4	2.45	29.9

The band gap energy (E_g) of g-C_3N_4, MIL-125(Ti) and the composites can be estimated, respectively, according to the Eq. (1) and the diagram is shown in Fig. 7(b).

$$\alpha h\nu = k\left(h\nu - E_g\right)^{1/n} \quad (1)$$

where k represents a constant, n is determined by the type of optical transition of a semiconductor. As displayed in Table 1, the band gap energy of CMTi reduces due to the coupling of g-C_3N_4 compared with pure MIL-125(Ti). As a result, the visible-light responses of CMTi composite are significantly improved. Meanwhile, the CMTi-2 has an E_g value of 3.24, which is the lowest than that of other composites. Photogenerated electrons and holes are easily separated in the transfer process, improving quantum efficiency greatly. In order to elucidate the fact that g-C_3N_4 and MIL-125(Ti) can cooperatively improve the separation of light-trigged charge carries, PL spectroscopy study has been performed. Fig. 8 presents the PL spectra of g-C_3N_4 MIL-125(Ti), and CMTi with an excitation wavelength of 320 nm [51]. Pure g-C_3N_4 has a strong peak around 440 nm in the PL spectrum, which can be attributed to the band gap

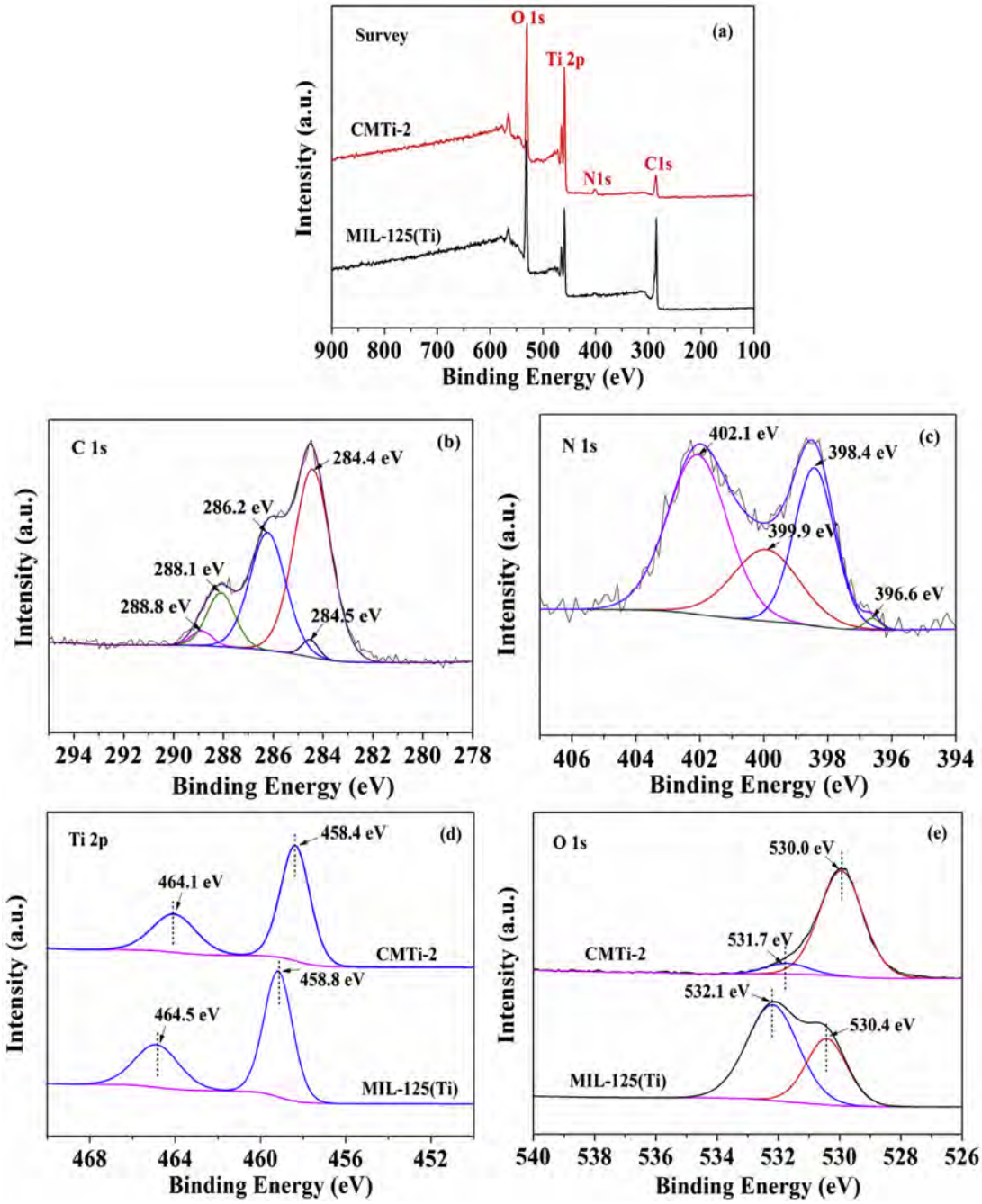

Fig. 5. The XPS spectra of CMTi-2 sample: (a) survey scan, (b) C 1s, (c) N 1s, (d) Ti 2p, and (e) O 1s. For comparison, the survey scan, Ti 2p and O 1s of MIL-125(Ti) sample are also shown.

recombination of electron–hole pairs. Comparatively, the PL intensity of CMTi weakens significantly, suggesting that the recombination rate of the photo-generated electrons and holes slow down for the composite [52]. In as-prepared CMTi composites, CNTi-2 possesses the lowest recombination rate of photo-generated electron–hole (e^-–h^+) pairs.

3.5. Dyes removal

Before degradation experiments, the rates of adsorption progress in samples have been tested. The hybrids exhibits enhanced adsorption capacity in contrast to pure MIL-125(Ti) and g-C_3N_4, as shown in Table 1. The RhB adsorption may not only result from simply physical adsorption but also form the conjugation between RhB and g-C_3N_4. Aromatic molecules like RhB could be adsorbed on the g-C_3N_4 surface with offset face to face orientation *via* π–π conjugation until an adsorption–desorption equilibrium is obtained [23]. The RhB photodegradation *via* the as-prepared CMTi composite are evaluated under visible-light irradiation ($\lambda > 420$ nm) (Fig. 9). For comparison, pure g-C_3N_4 and MIL-125(Ti) are also tested under the same conditions, which can degrade 81.3% and 10.1% RhB within 60 min, respectively. Considering that MIL-125(Ti) can not absorb the light with $\lambda > 420$ nm, the observed activity may be due to the dye-sensitization effect, since the colored RhB dye usually absorb visible-light [53]. All of CMTi hybrids exhibit higher photocatalytic activity than that of both MIL-125(Ti) and g-C_3N_4, indicating the synergistic effect between MIL-125(Ti) and g-C_3N_4 as obtained by chemical synthesis. The

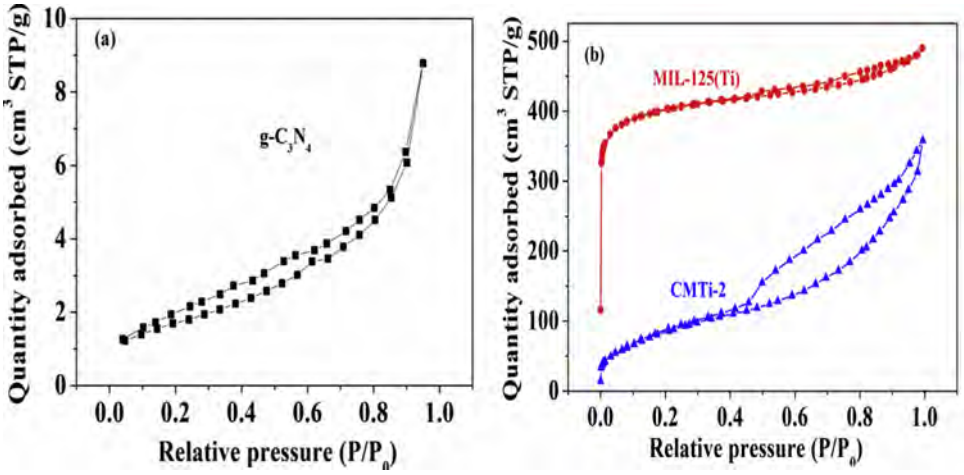

Fig. 6. N_2 adsorption–desorption isotherms of (a) g-C_3N_4 and (b) MIL-125(Ti), CMTi-2.

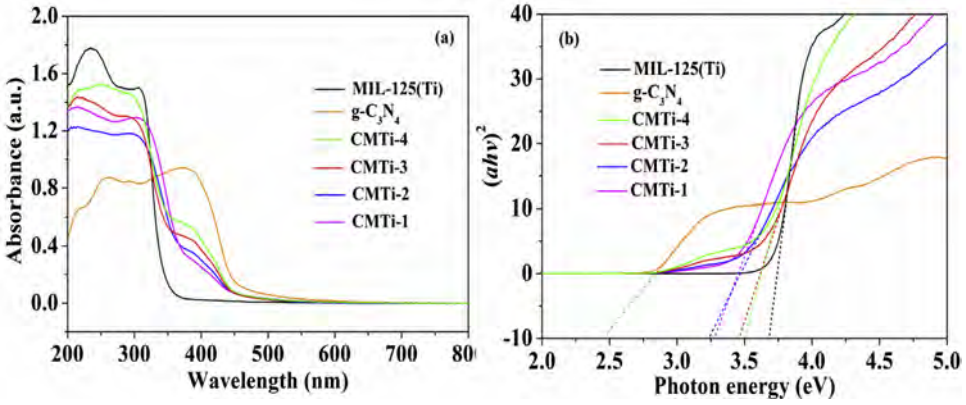

Fig. 7. UV–vis spectrum and (b) plot of $(\alpha hv)^2$ *vs.* photon energy (hv) of CMTi composite. For comparison, the thermal analysis for pure g-C_3N_4 and MIL-125(Ti) are also shown.

mesoporous CMTi-2 sample obtains the highest photocatalytic activity, which can degrade 95.2% of RhB after reaction within 60 min.

The kinetic curves for RhB photodegradation over CMTi photocatalysts are plotted according to the pseudo-first order model ($\ln(C/C_0) = kt$) and the values of k are shown in Fig. 10. The order of RhB degradation rate for as-prepared photocatalysts is CMTi-2 ($0.0624\,min^{-1}$) > CMTi-1 ($0.0581\,min^{-1}$) > CMTi-3 ($0.0528\,min^{-1}$) > CMTi-4 ($0.0515\,min^{-1}$) > g-C_3N_4 ($0.0299\,min^{-1}$) > mechanically mixed CMTi-2 ($0.0068\,min^{-1}$) > MIL-125(Ti) ($0.0026\,min^{-1}$). It is noteworthy that with the increase of g-C_3N_4 content, photocatalytic activity of CMTi hybrids shows a rise first followed by a decline. Increasing the content of g-C_3N_4 will not only benefit for charge transfer at the heterojunction interfaces, but also enhance the visible-light absorption (Fig. 6(a)). However, excess g-C_3N_4 may decrease the quality of effective heterointerfaces in CMTi, which is unfavorable

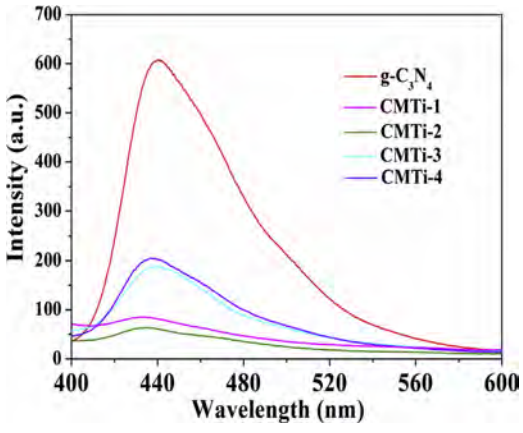

Fig. 8. Photoluminescence spectra of g-C_3N_4 and CMTi composites.

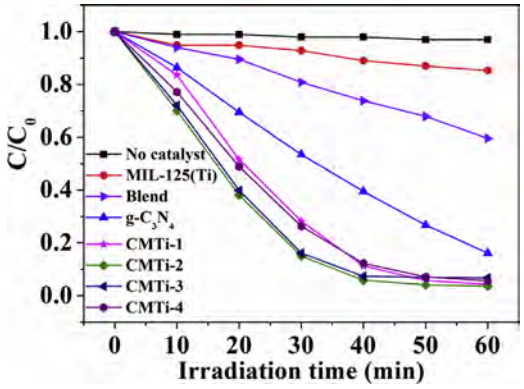

Fig. 9. RhB degradation photocatalytic performance of g-C_3N_4, MIL-125(Ti) and CMTi composites. For comparison, photocatalytic performance for no catalyst is also given. The "Blend" represents the sample of mechanically blending of MIL-125(Ti) and g-C_3N_4 with the g-C_3N_4 content of 7 wt%.

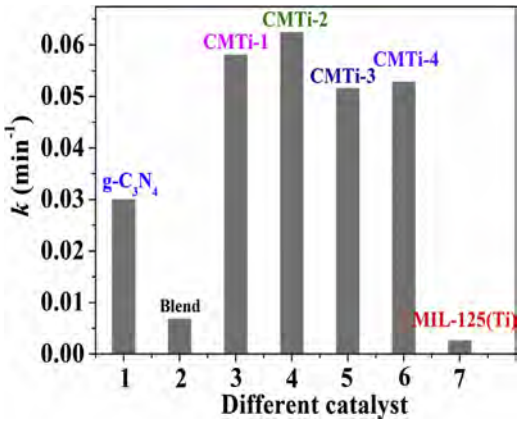

Fig. 10. The rate constant k of g-C_3N_4, MIL-125(Ti), blend sample and CMTi composites.

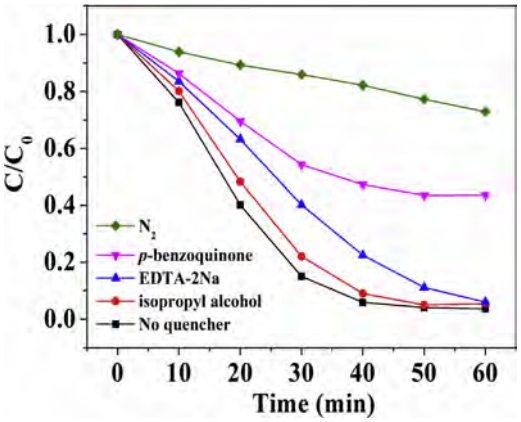

Fig. 11. Effects of different reactive species scavengers on the photodegradation of RhB by CMTi-2 under visible-light irradiation.

for the charge transfer at heterointerfaces [25]. To investigate the contribution of heterojunction structure between g-C_3N_4 and MIL-125(Ti) for RhB degradation, a control sample that has the same weight ratio of CMTi-2 had also been prepared by a physical blend method. The activity of physically mixed sample is still much lower than that of CMTi-2, indicating the interfacial interaction of both two components in the hybrids is much efficient than that in physical mixture for photocatalytic reaction. Further, the effect of RhB concentration for the photocatalytic activity of CMTi-2 has been carried out. The degradation efficiency of CMTi-2 for different initial RhB concentrations (30 mg/L, 50 mg/L, 70 mg/L, and 100 mg/L) are 99.1%, 95.2%, 70.5%, and 51.3%, respectively. This negative effect can be described to that the increase in dye concentration also decreases the path length of the photon entering the dye solution. Meanwhile, at high dye concentration a significant amount of solar light may be absorbed by the dye molecules rather than the photocatalyst and this may also reduce the photocatalytic rate. Similar results have been reported by Li et al. [55].Several reasons may account for this enhanced photodegradation activity. On the on hand, as the interphase spacers to g-C_3N_4 lamellar structure, the introduction of MIL-125(Ti) can prevent the agglomeration/restacking of g-C_3N_4 sheets and provide extra surface area to the photocatalyst, which improve the adsorption of pollutants in the liquid phase. What is more, the high surface-to-volume ratios of the composites will facilitate efficient transfer of electrons and holes to the surface of the material. The indirect dye photosensitization process may also be helpful for the improvement of RhB removal in the nanojunctions. The photocatalytic activity of CMTi-2 for degradation of colorless aqueous phenol and salicylic acid shows insignificant improvement compared with g-C_3N_4, the experiment results are not shown in this study. On the other hand, the opened mesoporous channels will not only make the active surface highly accessible to the RhB molecules, but also improve the mass transfer within the hybrid structure during photocatalytic process. More importantly, the synergistic effect between g-C_3N_4 and MIL-125(Ti), attributable to the heterostructures formation *via* the Ti—N bond, leads to an effective transfer of the photo-generated carriers during the photocatalytic reaction.

3.6. Photocatalytic mechanism

To evaluate the photodegradation mechanism, main oxidative species in the photocatalytic process were detected through radical and hole trapping experiments using EDTA-2Na (h^+ scavenger), *p*-benzoquinone ($^{\bullet}O_2^-$ scavenger), isopropyl alcohol ($^{\bullet}OH$ scavengers), or N_2 flow (excluding O_2) [26,54,56]. As shown in Fig. 11, the photocatalytic degradation of RhB is apparently restrained after the injection of EDTA-2Na, *p*-benzoquinone, or N_2. The rate constant reduces from 0.0624 min^{-1} in the photocatalytic system without any scavengers to 0.0152 min^{-1} or 0.0482 min^{-1}, when $^{\bullet}O_2^-$ is removed by *p*-benzoquinone or h^+ is removed by EDTA-2Na, respectively. The more the k value reduces the more important role

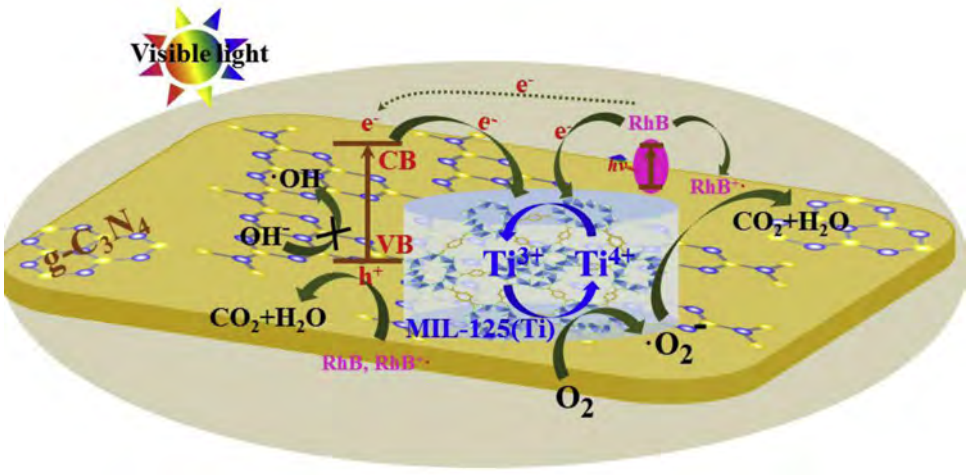

Fig. 12. Schematic of photo-generated charge carrier's separation and transfer in the CMTi system under visible-light irradiation.

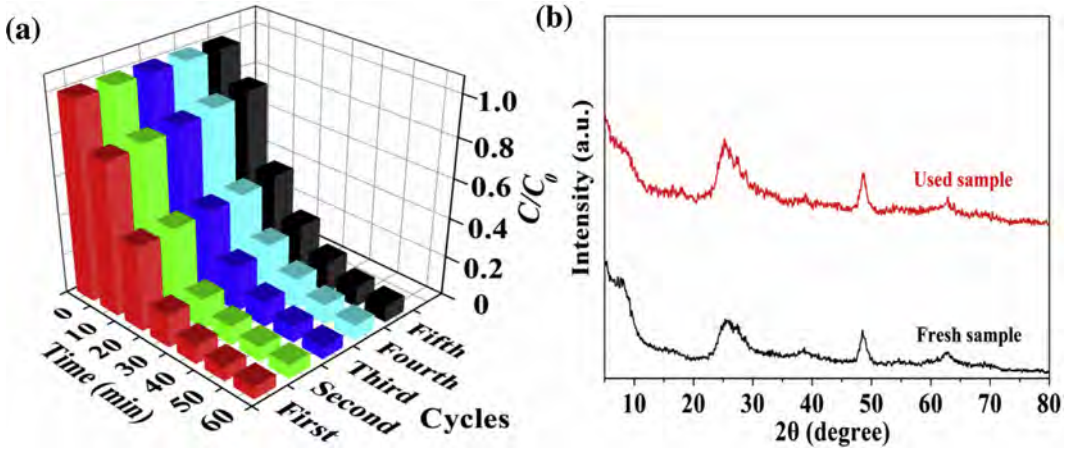

Fig. 13. (a) Recycling tests of CMTi-2 under solar light irradiation; (b) the XRD patterns of the CMTi-2 and the samples after five cycles.

the corresponding oxidative species plays in the reaction. However, ignorable inhibition is shown by isopropyl alcohol, implying the absence of •OH species. The results indicate that RhB degradation depends on both holes (h^+) and $^{\bullet}O_2^-$ greatly compared with •OH radical. To further prove the existence of $^{\bullet}O_2^-$, N_2 is purged through RhB solution to remove the dissolved O_2 in order to reduce radicals. The RhB degradation rate under N_2 is decreased to 0.0051 min^{-1}, which is much lower than that of EDTA-2Na and *p*-benzoquinone. It suggests that O_2 is the main factor for RhB photodegradation on CMTi photocatalysts, which affect the formation of $^{\bullet}O_2^-$ [57]. As a result, these reactive species (h^+ and $^{\bullet}O_2^-$) could efficiently degrade RhB dye into other products. Total organic carbon (TOC) test has been carried out to detect the carbon element in solution at different intervals over CMTi-2 and the results are shown in Fig. S1. After 60 min of irradiation, a relatively high mineralization rate of 90% TOC removal is obtained, indicating that RhB is mainly mineralized to CO_2 and water.

The photo-induced holes of g-C_3N_4 cannot oxidize the adsorbed H_2O molecules to •OH, since the value band potential of g-C_3N_4 (+1.6 eV *vs.* NHE) is more negative than the standard redox potential E^0(•OH/H_2O) (+2.8 eV *vs.* NHE). The adsorption of RhB on the photocatalyst surface is important when the photocatalytic degradation is initiated by the direct holes oxidation. And visible-light photocatalysis involves the indirect dye photosensitization and the excited electrons induced superoxide radical anions ($^{\bullet}O_2^-$). The dye molecules are easily captured on the surface of the photocatalyst owning to the hybrid induced high surface area and mesoporous structure. The adsorbed RhB are transferred into its excited state (RhB*) under visible-light irradiation. Then the electrons are injected from the RhB* into photocatalyst to form $RhB^{+\bullet}$. Moreover, g-C_3N_4 could also be excited from the value band (VB) to the conduction band (CB) under visible-light illumination. Both g-C_3N_4 and RhB can produce electrons under visible-light irradiation, which has also been demonstrated by Zhang et al. [58]. As discussed above, a plausible photocatalytic process has been schematized in Fig. 12. The photo-generated electrons originated from RhB or g-C_3N_4 transfer to the Ti^{4+} in the titanium–oxo cluster of MIL-125(Ti) due to the adsorption or the heterojunction structure. Ti^{4+} is thus, reduced to Ti^{3+}. Oxygen molecules adsorbed onto porous MIL-125(Ti) form superoxide ($^{\bullet}O_2^-$) ion radicals *via* electron transfer from Ti^{3+} to O_2 molecules due to the strong reducing ability of Ti^{3+} (−1.37 V *vs.* SHE). The Ti^{3+} ions are oxidized and further convert to Ti^{4+} ions. The electrons transportation in the titanium–oxo clusters of MIL-125(Ti) *via* the presence of Ti^{3+}–Ti^{4+} intervalence electron transfer had been demonstrated by previous reports [32,33]. The formed $^{\bullet}O_2^-$ radicals could efficiently degrade RhB (or $RhB^{+\bullet}$) into CO_2 and water. Simultaneously, the generated holes of g-C_3N_4 are capable of oxidizing RhB directly [26]. The above process can be summarized by the following multi-stage reaction:

$$RhB + h\nu \rightarrow RhB^* \rightarrow RhB^{+\bullet} + e^- \quad (1)$$

$$g - C_3N_4 + h\nu \rightarrow g - C_3N_4\left(e^- + h^+\right) \quad (2)$$

$$MIL - 125\,(Ti) + e^- \rightarrow Ti^{3+} - MIL - 125\,(Ti) \quad (3)$$

$$Ti^{3+} - MIL - 125\,(Ti) + O_2 \rightarrow Ti^{4+} - MIL - 125\,(Ti) + {}^{\bullet}O_2^- \quad (4)$$

$$^{\bullet}O_2^- + RhB/RhB^{+\bullet} \rightarrow \text{other products} \rightarrow CO_2 + H_2O \quad (5)$$

$$h^+ + RhB/RhB^{+\bullet} \rightarrow \text{other products} \rightarrow CO_2 + H_2O \quad (6)$$

3.7. Recyclability and stability

The recycle experiments of CMTi-2 for photocatalytic reaction under simulated solar light was carried out to evaluate the optical stability of the catalyst. As shown in Fig. 13(a), about 91.7% of RhB is still degraded after five runs, indicating that the CMTi-2 has insignificant loss of photocatalytic performance after five recycling runs. It is suggested that CMTi-2 keeps its photocatalytic performance without distinct photocorrosion during the oxidation of pollutant. In addition, the XRD pattern of the CMTi-2 after five times reuse is also shown in Fig. 13(b). No significant differences in the diffraction peaks are observed, demonstrating a very stable crystal structure. As a results, CMTi-2 can be used as efficient visible-light photocatalyst for application in wastewater treatment.

4. Conclusion

Highly active g-C_3N_4/MIL-125(Ti) hybrids with large surface area, mesoporous heterostructures, thermal stability, and enhanced visible-light absorption were successfully prepared on the basis of solvothermal strategy where g-C_3N_4 acted as the supporter for the formation of heterostructures. The heterostructures photocatalyst exhibited an improved photocatalytic performance for the degradation of Rhodamine B under visible-light irradiation. The photodegradation rate of RhB on g-C_3N_4/MIL-125(Ti) composites with the g-C_3N_4 content of 7.0 wt% was 0.0624 min^{-1}, about 2.1 and 24 times higher than that of pure g-C_3N_4 and MIL-125(Ti), respectively. The improved photocatalytic performance was ascribed to the indirect dye photosensitization, the Ti^{3+}–Ti^{4+} intervalence electron transfer and the synergistic effect between MIL-125(Ti) and g-C_3N_4. Cyclic experiments also indicated the reusability and stability of photocatalysts for the dye degradation. However, since the performance of MOFs can be readily tuned by differing the constituent metal ions and bridging organic

linkers, more high-efficiency metal-free semiconductor/MOFs photocatalysts will be expected for the applications of environmental remediation.

Acknowledgments

The authors gratefully acknowledge the financial support provided by the National Natural Science Foundation of China (nos. 71431006, 21276069, and 71221061), the Hunan Province Innovation Foundation for Postgraduate (no. CX2014B142).

Appendix A. Supplementary data

Supplementary data associated with this article can be found, in the online version, at http://dx.doi.org/10.1016/j.apcatb.2015.03.037.

References

[1] T. Li, L. Zhao, Y. He, J. Cai, M. Luo, J. Lin, Appl. Catal. B: Environ. 129 (2013) 255–263.
[2] M. Wen, K. Mori, T. Kamegawa, H. Yamashita, Chem. Commun. 50 (2014) 11645–11648.
[3] J. He, Z. Yan, J. Wang, J. Xie, L. Jiang, Y. Shi, F. Yuan, F. Yu, Y. Sun, Chem. Commun. 49 (2013) 6761–6763.
[4] J. Sun, G. Chen, J. Wu, H. Dong, G. Xiong, Appl. Catal. B: Environ. 132–133 (2013) 304–314.
[5] H.K. Chae, D.Y. Siberio-Perez, J. Kim, Y. Go, M. Eddaoudi, A.J. Matzger, M. O'Keeffe, O.M. Yaghi, Nature 427 (2004) 523–527.
[6] S. Horike, S. Shimomura, S. Kitagawa, Nat. Chem. 1 (2009) 695–704.
[7] E. Barea, C. Montoro, J.A.R. Navarro, Chem. Soc. Rev. 43 (2014) 5419–5430.
[8] B. Van de Voorde, B. Bueken, J. Denayer, D. De Vos, Chem. Soc. Rev. 43 (2014) 5766–5788.
[9] C.C. Wang, J.R. Li, X.L. Lv, Y.Q. Zhang, G.S. Guo, Energy Environ. Sci. 7 (2014) 2831–2867.
[10] L. He, Y. Liu, J. Liu, Y. Xiong, J. Zheng, Y. Liu, Z. Tang, Angew. Chem. Int. Ed. 52 (2013) 3741–3745.
[11] T. Kundu, S. Mitra, P. Patra, A. Goswami, D.D. Diaz, R. Banerjee, Chem.-A Eur. J. 20 (2014) 10514–10518.
[12] W.W. Zhan, Q. Kuang, J.Z. Zhou, X.J. Kong, Z.X. Xie, L.S. Zheng, J. Am. Chem. Soc. 135 (2013) 1926–1933.
[13] S. Abedi, A. Morsali, ACS Catal. 4 (2014) 1398–1403.
[14] Z.Q. Li, A. Wang, C.Y. Guo, Y.F. Tai, L.G. Qiu, Dalton Trans. 42 (2013) 13948–13954.
[15] C.-F. Zhang, L.-G. Qiu, F. Ke, Y.-J. Zhu, Y.-P. Yuan, G.-S. Xu, X. Jiang, J. Mater. Chem. A 1 (2013) 14329.
[16] K. Jayaramulu, V.M. Suresh, T.K. Maji, Dalton Trans. 44 (2015) 83–86.
[17] G. Lu, S.Z. Li, Z. Guo, O.K. Farha, B.G. Hauser, X.Y. Qi, Y. Wang, X. Wang, S.Y. Han, X.G. Liu, J.S. DuChene, H. Zhang, Q.C. Zhang, X.D. Chen, J. Ma, S.C.J. Loo, W.D. Wei, Y.H. Yang, J.T. Hupp, F.W. Huo, Nat. Chem. 4 (2012) 310–316.
[18] J. He, J.Q. Wang, Y.J. Chen, J.P. Zhang, D.L. Duan, Y. Wang, Z.Y. Yan, Chem. Commun. 50 (2014) 7063–7066.
[19] A. Aijaz, A. Karkamkar, Y.J. Choi, N. Tsumori, E. Ronnebro, T. Autrey, H. Shioyama, Q. Xu, J. Am. Chem. Soc. 134 (2012) 13926–13929.
[20] W.N. Zhang, G. Lu, C.L. Cui, Y.Y. Liu, S.Z. Li, W.J. Yan, C. Xing, Y.R. Chi, Y.H. Yang, F.W. Huo, Adv. Mater. 26 (2014) 4056–4060.
[21] Q.L. Zhu, J. Li, Q. Xu, J. Am. Chem. Soc. 135 (2013) 10210–10213.
[22] Y. Wu, H. Luo, H. Wang, RSC Adv. 4 (2014) 40435–40438.
[23] L. Gu, J. Wang, Z. Zou, X. Han, J. Hazard. Mater. 268 (2014) 216–223.
[24] S. Hu, L. Ma, J. You, F. Li, Z. Fan, F. Wang, D. Liu, J. Gui, RSC Adv. 4 (2014) 21657.
[25] L. Sun, Y. Qi, C.J. Jia, Z. Jin, W. Fan, Nanoscale 6 (2014) 2649–2659.
[26] L. Shi, L. Liang, J. Ma, F. Wang, J. Sun, Catal. Sci. Technol. 4 (2014) 758.
[27] K. Sridharan, E. Jang, T.J. Park, Appl. Catal. B: Environ. 142–143 (2013) 718–728.
[28] Y.B. Li, H.M. Zhang, P.R. Liu, D. Wang, Y. Li, H.J. Zhao, Small 9 (2013) 3336–3344.
[29] C. Pan, J. Xu, Y. Wang, D. Li, Y. Zhu, Adv. Funct. Mater. 22 (2012) 1518–1524.
[30] S. Wang, J. Lin, X. Wang, Phys. Chem. Chem. Phys. 16 (2014) 14656–14660.
[31] M. Dan-Hardi, C. Serre, T. Frot, L. Rozes, G. Maurin, C. Sanchez, G. Férey, J. Am. Chem. Soc. 131 (2009) 10857–10859.
[32] Y. Fu, Y. Chen, R. Huang, Z. Ding, X. Fu, Z. Li, Angew. Chem. 124 (2012) 3420–3423.
[33] H. Wang, X. Yuan, Y. Wu, G. Zeng, X. Chen, L. Leng, Z. Wu, L. Jiang, H. Li, J. Hazard. Mater. 286 (2015) 187–194.
[34] C.H. Hendon, D. Tiana, M. Fontecave, C. Sanchez, L. D'arras, C. Sassoye, L. Rozes, C. Mellot-Draznieks, A. Walsh, J. Am. Chem. Soc. 135 (2013) 10942–10945.
[35] M.A. Nasalevich, M.G. Goesten, T.J. Savenije, F. Kapteijn, J. Gascon, Chem. Commun. 49 (2013) 10575–10577.
[36] C. Petit, T.J. Bandosz, Adv. Mater. 21 (2009) 4753–4757.
[37] C. Petit, T.J. Bandosz, Adv. Funct. Mater. 21 (2011) 2108–2117.
[38] M. Jahan, Q. Bao, J. Yang, K.P. Loh, J. Am. Chem. Soc. 132 (2010) 14487–14495.
[39] Y. Zhang, G. Li, H. Lu, Q. Lv, Z. Sun, RSC Adv. 4 (2014) 7594.
[40] M. Jahan, Z. Liu, K.P. Loh, Adv. Funct. Mater. 23 (2013) 5363–5372.
[41] W. Ma, D. Han, M. Zhou, H. Sun, L. Wang, X. Dong, L. Niu, Chem. Sci. 5 (2014) 3946.
[42] V. Stengl, S. Bakardjieva, T.M. Grygar, J. Bludska, M. Kormunda, Chem. Cent. J. 7 (2013) 41.
[43] F. Sordello, G. Zeb, K. Hu, P. Calza, C. Minero, T. Szkopek, M. Cerruti, Nanoscale 6 (2014) 6710–6719.
[44] N. Boonprakob, N. Wetchakun, S. Phanichphant, D. Waxler, P. Sherrell, A. Nattestad, J. Chen, B. Inceesungvorn, J. Colloid Interface Sci. 417 (2014) 402–409.
[45] X. Zhou, F. Peng, H. Wang, H. Yu, Y. Fang, Chem. Commun. 47 (2011) 10323–10325.
[46] W.K.W. Scott, W. Rosencrance, N. Winograd, D.A. Shirley, Surf. Sci. Spectra 2 (1993) 71–75.
[47] D. Meng, J. Sun, S. Jiang, Y. Zeng, Y. Li, S. Yan, J. Geng, Y. Huang, J. Mater. Chem. 22 (2012) 21583.
[48] Y.Q. Wang, X.J. Yu, D.Z. Sun, J. Hazard. Mater. 144 (2007) 328–333.
[49] Z. Guo, W. Zhang, L. Zhou, H. Li, H. Wang, C. Andreazza-Vignolle, P. Andreazza, D. Zhao, Y. Wu, Q. Wang, T. Zhang, K. Jiang, ACS Appl. Mater. Interfaces 6 (2014) 20700–20708.
[50] G. Shao, T. Ma, X. Zhang, T. Ren, Z. Yuan, J. Mater. Sci. 44 (2009) 6754–6763.
[51] Z. Tong, D. Yang, T. Xiao, Y. Tian, Z. Jiang, Chem. Eng. J. 260 (2015) 117–125.
[52] Y. Zang, L. Li, X. Li, R. Lin, G. Li, Chem. Eng. J. 246 (2014) 277–286.
[53] L. Ge, C. Han, J. Liu, Y. Li, Appl. Catal. A: Gen. 409–410 (2011) 215–222.
[54] M. Najam Khan, M. Al-Hinai, A. Al-Hinai, J. Dutta, Ceram. Int. 40 (2014) 8743–8752.
[55] Y. Li, C. Wei, Catal. Sci. Technol. 1 (2011) 802–809.
[56] S. Kumar, A. Baruah, S. Tonda, B. Kumar, V. Shanker, B. Sreedhar, Nanoscale 6 (2014) 4830–4842.
[57] X. Li, J. Zhu, H. Li, Appl. Catal. B: Environ. 123–124 (2012) 174–181.
[58] W. Zhang, Y. Sun, F. Dong, W. Zhang, S. Duan, Q. Zhang, Dalton Trans. 4 (3) (2014) 12026–12036.